Spectral Performance and Calibration of the Suomi NPP OMPS Nadir Profiler Sensor

C. Pan[1] , F. Weng[2], and L. Flynn[2]

[1]ESSIC, University of Maryland, College Park, MD, USA, [2]NOAA Center for Satellite Research and Applications, College Park, MD, USA

Abstract The Ozone Mapping and Profiler Suite (OMPS) is one of five instruments on board the Suomi National Polar-orbiting Partnership (Suomi NPP) satellite. As part of OMPS, the Nadir Profiler (NP) spectrometer measures Earth's albedo in ultraviolet wavelengths from 250 to 310 nm to profile Earth atmospheric ozone concentration. Since launch in 2011, many changes in the NP radiometric and spectrometric calibration have been made to improve sensor data quality. The most challenging issue is to characterize instrument on-orbit spectral calibration and to maintain a stable spectral performance to meet sensor design criteria. Validation of the NP sensor data found an average of 3–5% error in the sensor albedo measurements that exceeded 2% requirement, creating 1–2% uncertainty in ozone profile. Data analysis attributes the error to prelaunch calibration uncertainty, ground-to-orbit dichroic changes, and on-orbit detector wavelength registration drifts. A recent update of calibration significantly improved spectral wavelength knowledge as well as the accuracy of the measured solar spectra. As a result, the wavelength-dependent albedo error is significantly reduced and generally meets the radiometric uncertainty requirement of 2%.

1. Introduction

The Ozone Mapping and Profiler Suite (OMPS) Nadir Profiler (NP) is an advanced radiation spectrometer (Dittman et al., 2002; Rodriguez et al., 2003) which is designed to measure backscattered ultraviolet (BUV) sunlight at the top of the Earth atmosphere, providing estimates of the Earth atmospheric ozone concentrations with a 4 day revisit (Pan, Kowalewski, et al., 2013). As a bridge between the U.S. National Oceanic and Atmospheric Administration (NOAA) Polar Orbiting Environmental Satellites (POES) and Joint Polar Satellite Systems (JPSS), the first OMPS flight unit is flying on NOAA's Suomi National Polar-orbiting Partnership (S-NPP) satellite launched in October 2011. The following three OMPS flight units will fly on a series of JPSS satellites. OMPS mission objective is to provide continuity with global ozone data for operational remote sensing of weather and other environmental applications.

sUtilizing the BUV technique, NP estimates ozone profile through measurements of incoming UV light (irradiance) and backscattered UV light (radiance) in 250–310 nm range at a spectral resolution of 1.0 nm. A ratio of radiance to irradiance, so-called normalized radiance (NR), in which sensor effects as well as solar flux changes cancel, is the primary input to the ozone retrieval algorithms. By deploying two solar diffusers, NP performs in-flight spectral calibration and maintains calibration stability through a time series of solar spectra measurements (Pan & Flynn, 2015). While the most important attributes in NP calibration are detector performance, internal stray light correction, and spectral wavelength knowledge, the most important aspects that degrade the NP performance are (1) unexpected NP dichroic filter shift during sensor transition from ground to orbit, (2) on-orbit detector spectral drifts exceeding sensor design criteria of 0.018 nm, and (3) working diffuser degradation impact as well as solar activity influence; all of the three effects must be corrected in ground data processing system. Validation of the calibration is conducted via an intersensor comparison between the NP and the well-calibrated Nadir Mapper (NM) flying on the same satellite. This paper discusses the NP in-flight spectral performance and calibration, explains the underlying optical mechanism, and demonstrates a successful calibration change that has significantly improved albedo calibration accuracy.

2. Nadir Profile Instrument

NP radiation spectrometer is a double spectrometer based on a double Monk-Gillieson monochromator design. Figure 1 shows optical layout of the system where light enters a telescope in either Earth
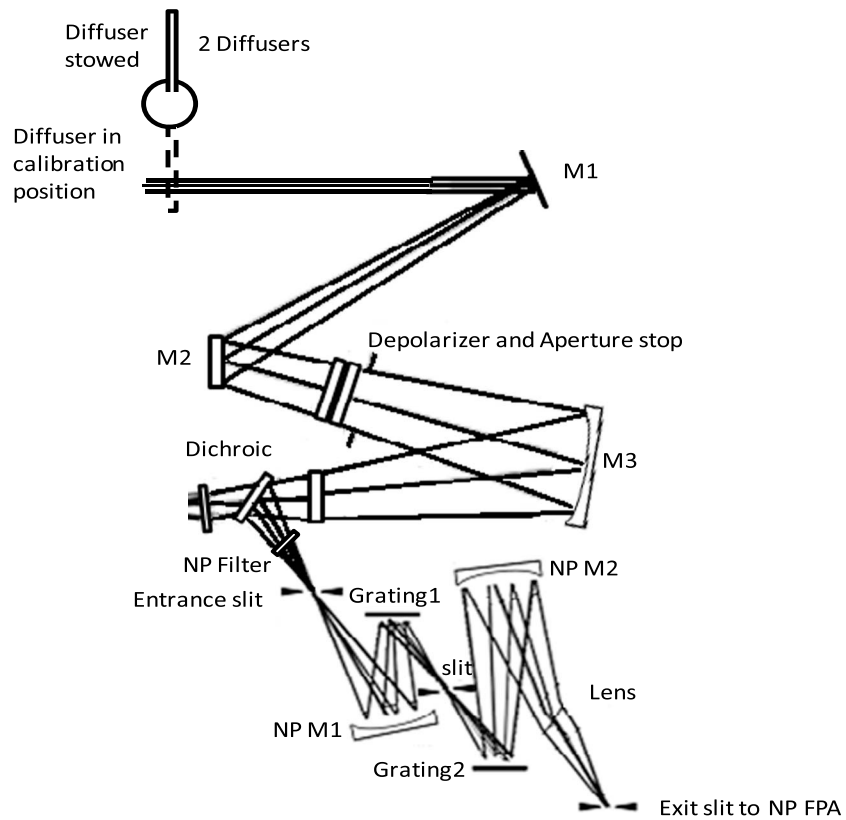
Figure 1. A diagram of the Nadir Profiler instrument optical layout.

observation or solar calibration mode. In Earth observation, light enters directly into the telescope and the first reflection is off the Mirror 1 (M1) optic. While in calibration mode, the reflective diffuser is deployed and the first bounce is off of the diffuser and then the M1 optic. Beyond the M1 optic, the light path is shared by Earth view and calibration view. Light entering the telescope is split by a dichroic beam splitter to reflect most of the 250–310 nm light to the NP radiation spectrometer, then the light is dispersed by a grating system and focused onto a 2-D spectral-spatial CCD detector focal plane assembly (FPA). The FPA comprises an optical detector array of 390 individual spatial pixel rows and 340 spectral pixel columns, but only a subregion of 93 spatial pixels by 147 spectral pixels is a photon sensitive region used to provide a response to photons within 250–310 nm. The spectral sampling on the detector is 2.4 pixels/nm. While the electronics system has flexible sampling and binning of pixels by summation, NP operation bins the 93 individual spatial pixels to create a single macropixel in science observation. Thus, an NP Earth view image functionally has one macropixel and 147 spectral channels to record its 16.6° cross-track field of view (FOV) measurements, covering a ground swath of 250 km and an along-track integration over 250 km (37.4 s total integration time). Table 1 summarizes the key parameters of NP CCD detectors and spectral properties.

3. Calibration

Like other BUV sensors, normalized radiance NR is a primary input to ozone retrieval algorithms to estimate ozone concentrations. Conceptually, calibration of measured Earth radiance and solar irradiance can be considered separately for an individual CCD pixel since the radiance and irradiance wavelength scales may differ. Solar observation provides band center wavelength scale for the observed solar spectra, while Earth spectral wavelengths are determined by extrapolating in time the band center wavelengths derived from solar wavelength calibrations just prior to the terrestrial observations.

NP ground system processes Earth spectral signals (in counts) by removing a number of offsets from the raw data prior to converting counts to radiances. Let $I_\lambda^m(t)$ be the time-dependent Earth radiance in the λ spectral

Table 1
OMPS Nadir Profiler (NP) Instrument Baseline Specifications

	Description
Orbit	On board Suomi NPP in Sun-synchronous orbit at 833 km altitude, 98.7° inclination with a nominal 13:30 local time ascending node
Telescope	One telescope feeds two separate grating CCD spectrometers
Swath width	250 km after pixel binning (2.7 km at nadir before binning)
Field of view (FOV)	16.7 × 0.25°
Spectral range	250 to 310 nm
Spectral sampling interval	2.4 pixels per nm
Spectral resolution	1.0 nm full width at half maximum (FWHM)
Detector cooling	Thermoelectric coolers (TECs)
	Operational set point: −45.0°C
Calibration	On board LEDs, linearity and gain correction, data binning, hot pixel removal, and working and reference reflective diffusers for periodic solar observations

channel; $C_{\lambda x}^{r}(t)$ be the offset corrected counts at pixel (λ, x); $k_{\lambda x}^{r}$ be the radiance calibration constant; and $\tau_{\lambda x}$ be the time-dependent pixel response changes, the measured Earth radiance then can be theoretically expressed in equation (1), where 93 spatial pixels are binned to a macropixel. Details on the NP signal offsets correction can be found in (Pan, Flynn, Wu, et al., 2014)

$$I_{\lambda}^{m}(t) = \sum_{x=1}^{x=93} \frac{C_{\lambda x}^{r} k_{\lambda x}^{r}}{\tau_{\lambda x}^{r}(t)} \tag{1}$$

Processing of measured solar data corrects the observed solar signal counts, $C_{\lambda x}$, for several instrument characteristics: nonlinearity of the sensor electronics system, diffuser bidirectional reflectance distribution function $BRDF_{\lambda x}$, electronics bias, CCD dark current, and CCD smear signal. The BRDF is a function of the incident zenith angle θ_s and azimuth angle ϕ_s of the light, as well as the viewing zenith angle θ_v and azimuth angle ϕ_v of the observer. Prelaunch ground measurement provided a 40 × 40 grid of BRDF values at varying azimuth and elevation angles for each detector pixel; linear interpolation of the grid at the actual solar observation angles may have errors up to 1% for individual pixels. The corrected solar measurement counts, $C_{\lambda x}^{i}$, are obtained for each pixel (λ, x):

$$C_{\lambda xjk} = C_{\lambda xjk}^{o} + C_{\lambda xjk}^{ir} \, BRDF_{\lambda xjk}(\theta_s, \phi_s, \theta_v, \phi_v), \tag{2}$$

where $C_{\lambda x}^{o}$ is an offset signal containing scattered light, dark current, smear, and electrical bias. Estimation of these offset signals can be found in Pan, Flynn, Buss, et al. (2014). The measured solar irradiance F^m at spectral channel λ can be written as a time-dependent function:

$$F_{\lambda}^{m}(t) = \sum_{x=1}^{N} \frac{C_{\lambda x}^{i} k_{\lambda x}^{i}}{\rho(t) \, \tau_{\lambda x}(t)}, \tag{3}$$

where $k_{\lambda x}^{i}$ is irradiance calibration constant corrected for wavelength shifts; $\rho(t)$ is the solar diffuser plate reflectivity ($\rho(t=0) = 1$); $\tau_{\lambda x}(t)$ is the sensor throughput changes ($\tau(t=0) = 1$); N is the number of CCD spatial pixels used in solar measurement; NR at spectral pixel j is expressed as

$$NR_{j}^{m} = \frac{I_{j}^{m}}{F_{j}^{m}} \tag{4}$$

Like other modern UV sensors, NP deploys solar diffusers to maintain on-orbit calibration stability by measuring a time series of solar spectra. A working diffuser is deployed bi-weekly, and a reference diffuser is used semiannually. The different exposure frequency of the two diffusers allows to determine both diffuser and instrument degradation from the two diffuser measurements (Pan & Flynn, 2015). NP solar measurements take place when Soumi-NPP satellite observatory crosses Earth northern terminator. The measurement collects nominally 17 images from an observation. Figure 2 shows an example of the solar image collected on 20 May 2017. The 140 spatial pixels and 209 spectral pixels were sampled and registered onto the CCD focal plan. Subsequent processing of each solar image is expressed in equations (2) and (3).
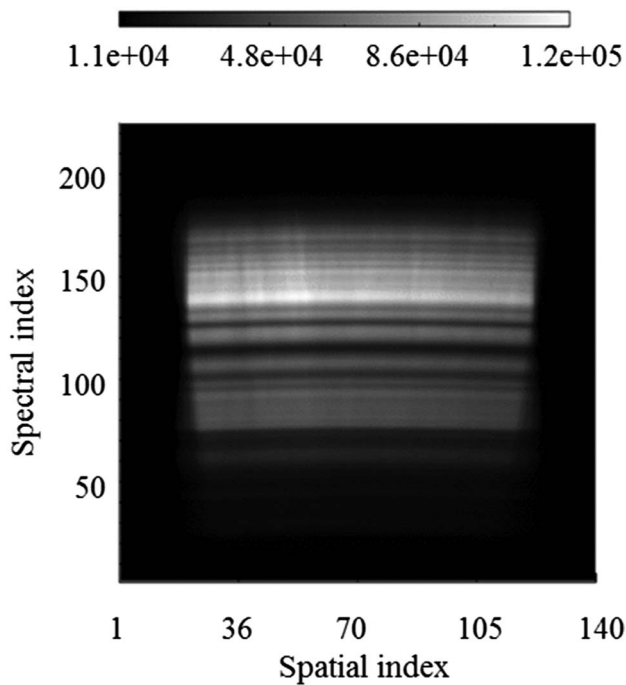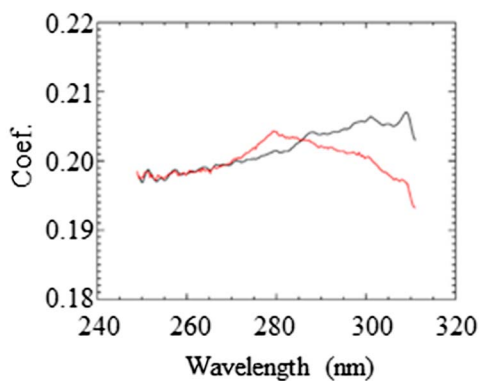
Figure 2. A measured NP solar raw image data on 20 May 2017 which contains two-dimensional spatial and spectral pixels of 140 × 209. A subarea (photon sensitive region) of 93 × 147 CCD pixels are used in ground data analysis. All spatial pixels are then averaged to form a macropixel for Earth radiance retrieval. Image intensity unit is counts.

4. Spectral Performance Evaluation
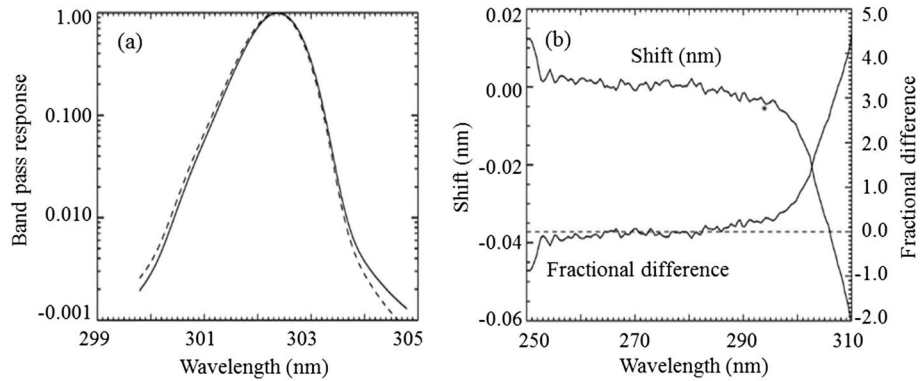
4.1. Dichroic Change

NP disperses spectra and registers spectral wavelength scales onto its photo detectors. There are two major error sources, in line with optics alignment and the optical dispersion, that affect spectral performance: changes in CCD pixel spectral wavelength registration and changes in the dichroic (beam splitter) filter's transmittance (Pan, Wu, et al., 2013). Reanalysis of data has confirmed that after launch, NP spectral wavelength registration has changed about −0.144 nm from its original lab measurement due to a nearly 25°C change in optical bench temperature between ground measurements and orbit. The change produces a 3%–10% radiometric error particularly on long wavelengths 300–310 nm where sensor responses change dramatically. The impact of the dichroic shift on NP ozone retrieval was up to 2.4% which is a combination effects from the wavelength change as well as dichroic filter transmittance change. Therefore, a recent correction is also made to the albedo calibration coefficient. Figure 3 shows the NP albedo calibration coefficients before (red) and after (black) the dichroic filter shift.

4.2. Instrument Degradation

Monitoring of on-orbit solar spectra changes, instrument throughput's changes as well as diffusers' degradation can be determined. Following the approach of heritage instruments, such as the Solar Backscatter Ultraviolet Radiometer-2 (SBUV/2) (Jaross et al., 1998), the working diffuser measurements provide information of exposure dependent diffuser degradation rate, while the infrequently exposed reference diffuser monitors instrument degradation after removal of the degradation effect of the diffuser itself. Details of the degradation assessment can be found in Pan and Flynn (2015). Recent estimation finds less than 1% degradation in NP instrument, but about 0.5–2.8% degradation in the working diffuser. Since the instrument degradation is largely removed in the NR calculation, only the working diffuser degradation in the solar irradiance calculation matters most to the NR measurements, which could causes up to 10% error if it is left uncorrected after 6 years of operation. Details can be found in section 4.6.

4.3. Spectral Response Function

Band passes determine spectral band center wavelengths and band spectral response. Error sources in the band-pass calibration attribute to ground calibration and on-orbit band-pass shape broadening. Ground calibration of the NP band passes took place in a laboratory, wherein the sensor views an integrating sphere illuminated by a frequency multiplied tunable laser at various wavelengths at a discrete number of azimuth positions. The test measured the band passes for selected wavelengths groups, and data processing interpolates the selected wavelength groups to all other pixels spectrally and spatially with an interpolation error of less than 0.5%. Analysis of the prelaunch data has demonstrated that the instrument is in compliance with both spectral resolution of FWHM ≤ 1.0 and channel isolation requirements. The band passes were normalized, and therefore, the absolute spectral dependence of the sensor's optical throughput was removed. Introduction of the instrument sensitivity is now made by convolving the normalized band passes with the instrument throughput. Figure 4a shows band-pass response change and center wavelength shifts before and after applying sensitivity correction on wavelength 302.3 nm as a typical example. Figure 4b shows the amount of band center wavelength change from −0.06 nm to 0.02 nm along the sensor spectral coverage that is a maximum of 4.5 fractional difference from the prelaunch data. The maximum

Figure 3. Albedo calibration coefficient (Coef.) change along NP wavelengths to account for dichroic filter transmission (red) before (from Ball Aerospace & Technologies) and (black) after dichroic change (from NASA). Coef. is a ratio of radiometric coefficient to the irradiance coefficient.

Figure 4. (a) Example of the band-pass change in 303.67 nm wavelength channel before (solid line) and after (dashed line) the correction of sensor optic throughputs. (b) Impact of band-pass error to band center wavelengths after applying the sensor optic throughputs.

change is found on longer wavelengths where sensor sensitivity dramatically increases by ~10% per nanometer. Calibration of on-orbit band-pass broadening is not significant in NP FWHM, but it is still considered as part of a combination of effects of wavelength registration change (addressed in the next section).

### 4.4. Wavelength Registration

Wavelength registration defines spectral band center wavelength scale on each CCD pixel detector. Calibration finds and corrects any changes of pixel spectral registration for Earth observation through solar measurements. Such spectral change is due to instrument temperature change and is in relation to changes in both optics alignment and dispersion. To quantify such changes, a synthetic spectrum $F^S(\lambda)$ at wavelength λ was constructed as a standard baseline for observed solar spectra. The synthetic spectrum is constructed by convolving of a high spectral resolution reference solar spectrum $I(\lambda)$ with the NP band passes $B(\lambda)$ corrected in the previous session.

$$F^S(\lambda) = \frac{\int I(\lambda)B(\lambda)\mathrm{d}\lambda}{\int B(\lambda)\mathrm{d}\lambda} \tag{5}$$

The high spectral resolution reference solar spectrum is composed of solar measurements from ATLAS SUSIM and Kitt Peak National Solar Observatory which has a 0.01 nm spectral resolution (Woods et al., 1996). Changes in the wavelength registration are then computed by comparing the synthetic spectrum with the actually observed spectra. A nonlinear regression with two basis parameters of additive δ and multiplicative
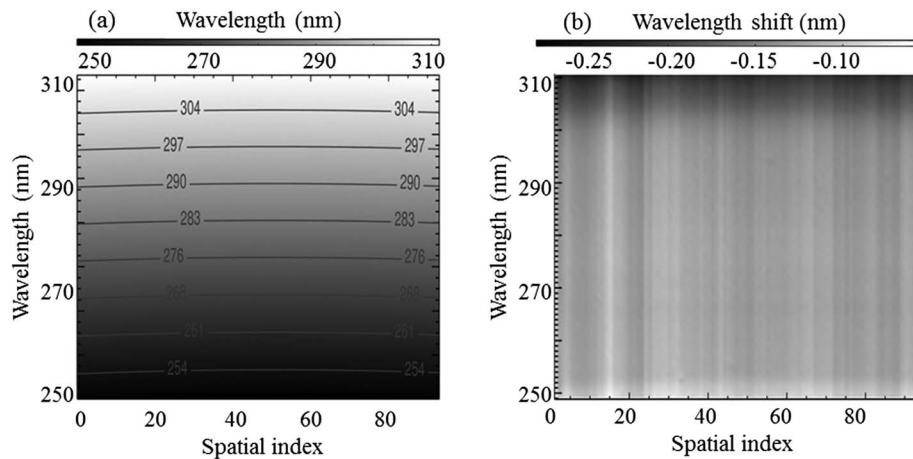
Figure 5. (a) Prelaunch lab defined wavelength registration on the effective NP CCD detector which has 93 spatial pixels and 147 spectral channels from 249 to 310 nm. (b) In-flight band center wavelength changes for the same CCD region due to a combination of effects of slit irregularity and thermal optical impacts.
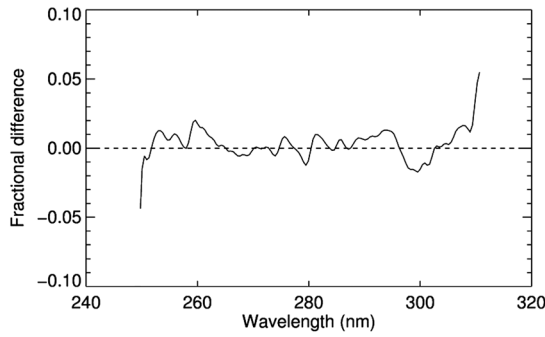
Figure 6. An example of a fractional difference between the synthetic solar spectrum and a measured solar spectrum on 19 February 2017. Difference between the two spectra indicates a shifted solar spectrum. Effects of solar activity and diffuser degradation were removed.

$P(\lambda)$ factors, representing spectral shift and dispersion, has been developed to establish and maintain detector pixel spectral registration. Varying the two parameters for a cubic scaling in wavelength of the reference spectra F^s (NOAA/STAR, 2014),

$$P(\lambda) = a + b\lambda + c\lambda^2 + d\lambda^3 \qquad (6)$$

Spectral shifts including band pass broadening effect are determined via a minimum chi-square statistic Δ_{min} over all wavelengths in common between the modeled F^s and the observed F^o spectra scaled by solar measurement noise σ.
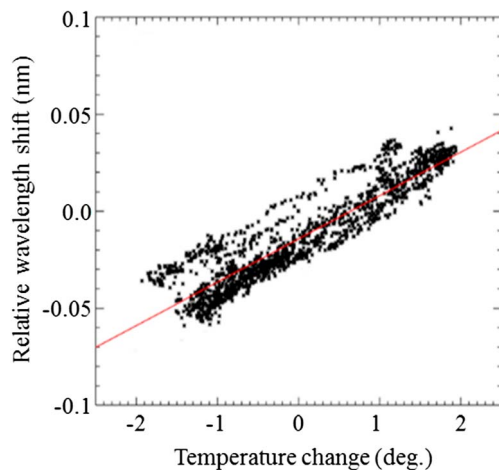
$$\Delta_{min} = \arg\min\left(\sum_{\lambda}\{(F^o(\lambda) - P(\lambda)\cdot F^s(\lambda + \delta))/\sigma\}^2\right). \qquad (7)$$

Changes in band center wavelength scale is time dependent. Figure 5a contours prelaunch defined wavelength registration on each CCD pixels in the CCD photo sensitive region. Slight distortions of the image on the CCD cause the pixel band center wavelengths to vary slowly ≤0.701 nm across the spatial dimension due to slit irregularities, resulting in unique spectral registration at each pixel spatial position. Figure 5b shows changes of the wavelength scale relative to the prelaunch data due to the combined effects of dichroic change, band pass change and in-flight pixel wavelength registration drifts. The in-flight data were collected on 19 February 2017.

Accuracy of the wavelength drift is evaluated by examining regression residuals as shown in Figure 6. About ±1% residual structure for wavelengths between 250 nm and 309 nm is typical of a characterization. Extrapolation to wavelengths shorter than 250 nm appears to be less accurate. The residual structure is often shared at different spatial locations on the detector, suggesting that they are caused by systematic sources of error such as radiometric calibration or in the solar reference spectrum.

4.5. Time Series Detector Spectral Drift

NP spectral wavelength scales are expected to drift with time in both solar and Earth spectra independently due to different measurement sequences and different viewing conditions Error budget requires the drift shall be less than 0.018 nm. However, both solar spectra and Earth spectra have shown a larger drift, adding additional 1% radiometric errors to the calibration if the drift is ignored. Root cause attributes the drift to the sensor thermal loading change which was largely ignored in the prelaunch budget analysis. Figure 7 demonstrates a cross correlation between Earth spectra wavelength shifts and the NP telescope temperature changes. Fourteen orbit Earth spectra were collected, and each orbit datum contains 80 individual Earth spectra which were processed separately so the result indicates intraorbit wavelength drifts, from −0.054 nm to 0.047 nm when telescope temperature changes from −2 to +2°C, about 0.03 nm per degree Celsius, at a cross-correlation coefficient of 98%. Minimization of intraorbit wavelength shifts is achievable if a calibration is applied on each Earth spectrum within an orbit.
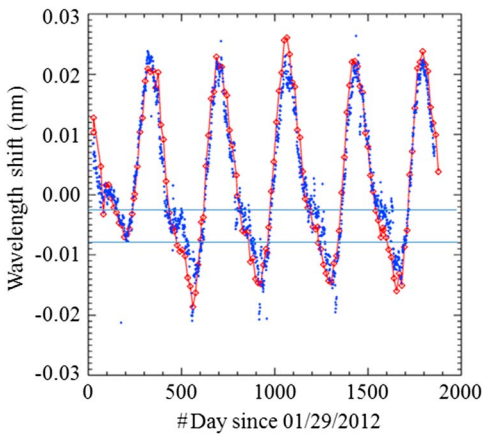

Figure 7. Correlation between the NP housing temperature change and the intraorbit Earth spectral wavelength variation. Data were collected from 1120 Earth spectra.

From examination of solar wavelength shifts from 120 solar spectra, 0.03 to 0.01 nm variation is observed as shown in Figure 8 is observed. The data have a clear annual pattern slightly smaller than the intraorbit drifts observed in Earth view spectra as shown in Figure 7. A calibration model predicts the annual wavelength shifts $\Delta\lambda$ as a function of time x (number of days of the year) relative to the very first solar observation. The model is modified from the previous study (Pan, Kowalewski, et al., 2013) and applied for 1 year data only at a time to extract a general trend. The fitting parameters have reduced by 40% while achieving a high degree of accuracy with an R-square goodness of 0.999 and root-mean-square (RMSE) of 0.0004.

$$\begin{aligned}\Delta\lambda(x) &= a1^*\sin(b1^*x - c1) + a2^*\sin(b2^*x - c2) \\ &\quad + a3^*\sin(b3^*x - c3).\end{aligned} \qquad (8)$$
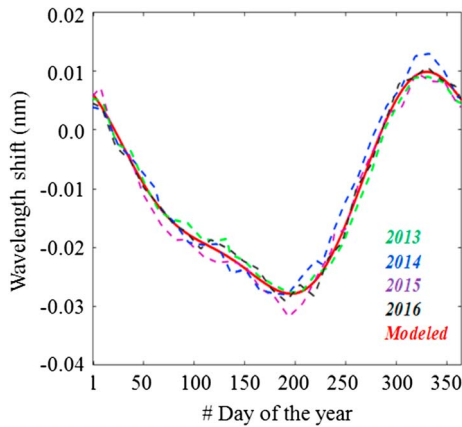
Figure 8. Annual pattern of wavelength variation from 2013 to 2016. The pattern is associated with the sensor thermal loading change caused by the annual variation of the spacecraft-centered solar azimuth angle, sometimes called the beta angle—the angle between the velocity vector and the solar direction. The red solid line is the modeled function fitted from the 4 year data. Data were collected from 150 solar measurements.

where *a*, *b*, and *c* are fitting coefficients applied to all the solar measured data separated by year. Interpolation of the data estimates a daily wavelength shift that reduces error to less than 0.005 nm, while extrapolation of the fitting in time forward predicts the amount of wavelength shifts for the next 2 weeks before adding newly measured solar data.

Earth spectra annual wavelength pattern is estimated via daily averaged Earth spectra. The averaging smooths out the intraorbit variation. Figure 9 plots solar wavelength annul patterns (blue) on top of the Earth spectra (red) variation. A small difference of <0.01 nm can be found between the two horizontal lines where the solar measurements took place around solar beta angles of 19° ± 0.2°, indicating a different viewing condition between Earth observations and solar measurements. Correction of such difference is made by adjusting the modeled wavelength to match the Earth spectra beta angles of 19°.
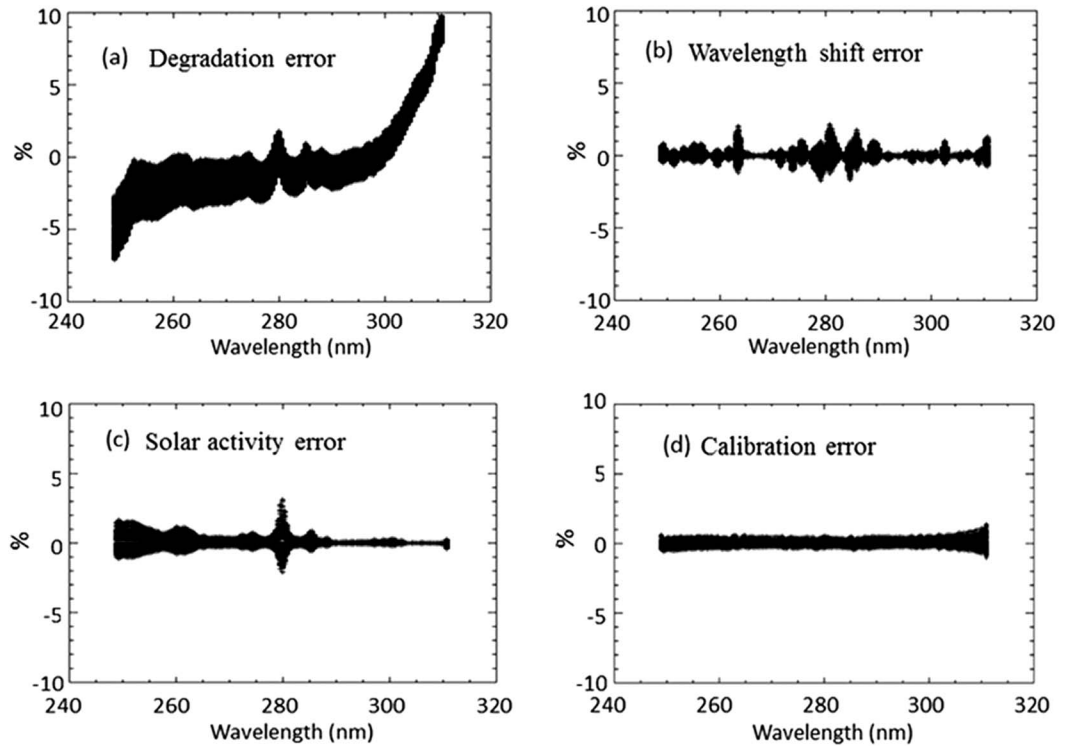
4.6. Errors and Uncertainties

For NP case, the primary factors that impact the spectral calibration accuracy are wavelength registration change, solar activity, and sensor throughput change. Quantification of these errors use a multivariable regression applied separately to Earth spectra as well as solar spectra to extract each individual liner trends. Regression with a smooth first-order polynomial for each solar spectra on a time series yields degradation rates of the two diffusers. Depending on exposure frequency, the working diffuser has a faster degradation rate than the reference diffuser. Subtracting the reference diffuser degradation from the working diffuser degradation, the working diffuser degradation is estimated at ~0.5% to 2.8% after 6 years of operation, creating up to 10% deviation in spectral calibration if no correction was applied (Figure 10a), especially at longer wavelengths. Errors from wavelength shifts are shown in Figure 10b; a percent difference between the wavelengths shifted spectra with the measured spectra is ±2.2%. The solar activity trending uses the magnesium Mg II core-to-wing ratio as a proxy (Heath & Schlesinger, 1986; Snow et al., 2014). The ratio cancels out most instrumental calibration factors, and the wavelength scale is precisely determined by fits to the photospheric absorption lines near the Mg II lines. The algorithm yields an uncertainty of 0.6%. Given the NP spectral resolution, three measurements $k = 1, 3$ from $I (k, t)$ in the core lines of 279.50, 279.92, and 280.35 nm and four measurements in two separate wing lines: $m = 1, 2$ from $I (m, t)$ (276.53 nm, 276.95 nm) and $n = 1, 2$ from $I (n, t)$ (282.90 nm, 283.32 nm) are used in the analysis for statistical robustness,

$$\text{Mg II}_0 (t) = \frac{4}{3} \sum_{k=1}^{3} I(k, t) / \left(\sum_{m=1}^{2} I(m, t) + \sum_{n=1}^{2} I(n, t) \right) \quad (9)$$

Change in the Mg II magnitude relative to the time-averaged Mg II value is used to scale spectral change, representing solar activity influences on the measured solar spectra. Estimation of error is less than ±2%, except for wavelengths around 280 nm where ozone absorption lines show a relatively larger uncertainty due to low signal-to-noise ratios. After correction for the combined effects of wavelength shifts, working diffuser degradation as well as solar activity, the accuracy of the observed solar spectra has improved from 6% (not shown in this paper) to less than ±1.8% as shown in Figure 10d.
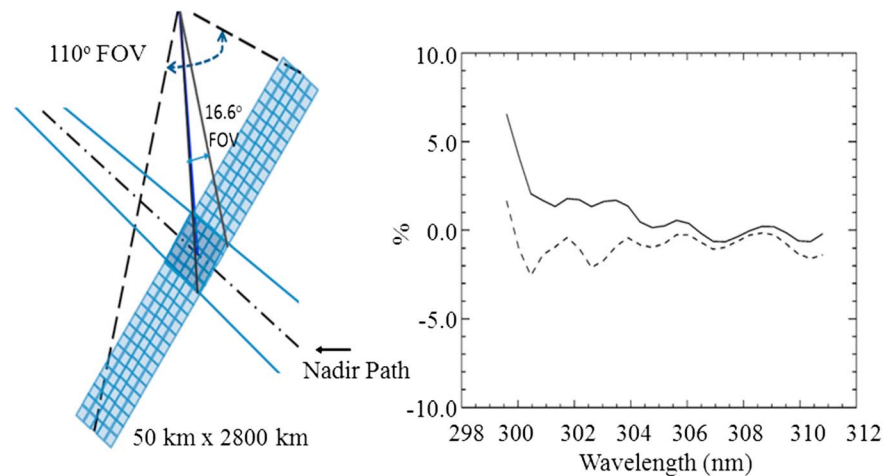
5. Intersensor Comparison

Validation of the current calibration is conducted via an intersensor NR comparison between OMPS Nadir Mapper (NM) and NP with a focus on the higher sensor sensitivity spectral region. OMPS NM is a well calibrated UV spectrometer with 1% or less radiometric calibration uncertainty within its nadir view of 16.6° (Pan et al., 2017) that is

Figure 9. Earth spectra (red) also have annual variation similar to the solar spectra (blue) variation in general. However, < 0.01 nm differences can be found between two spectra around beta angles of about 19° ± 0.2° bounded by the two horizontal lines. There is a small year-to-year variation caused by a solar beta angle change in the measurement viewing condition due to orbit inclination maneuvers intended to maintain the equator-crossing time near 1330 LT.

Figure 10. Errors estimated from a time series of measured solar spectra. (a) Degradation error from the working diffuser can be as large as 10%. (b) Band center shift errors are wavelength dependent and on the order of 2.2%. (c) Solar activity error. (d) Calibrated solar spectra error after correction for wavelength shift, solar activity, and the working diffuser degradation.

co-boresighted with the NP FOV to 0.1° (3 sigma level) accuracy. A comparison of NP and NM provides estimates of the NP data quality. Normally, NM and NP Earth spectra are acquired simultaneously through the same telescope aperture, overlapping spatially and spectrally in the 299 nm to 311 nm wavelength range at the same 1 nm spectral resolution. A single NP footprint matches five central NM instantaneous

Figure 11. (a) NP IFOV collocated with 5 cross-track × 5 along-track NM IFOVs in Earth observation with time match for an intersensor comparison. Each NM IFOV has a spatial resolution of 50 km × 50 km. One scan of NM measurement covers 2,800 km cross track and 50 km along track. The central gray region is the footprint of the collocation covering 250 km × 250 km square Earth area. (b) NP radiometric accuracy in NR up to 6% relative to the NM before the calibration (solid line) drops to an average of 0.8% after the calibration (dashed line). Data were collected globally from 1,100 Earth spectra on 1 July 2017. South Atlantic Anomaly region was excluded.

field of view elements (IFOVs) in the satellite cross-track direction (Figure 11a), and NP Earth view integration of 37.4 s coincides with five successive NM swaths along track in the NP FOV. The comparison also time matches NP spectra with NM subspectra at the same wavelengths by linearly interpolating the NP data to the NM wavelength scale. More than 800 spectra data sets from a global coverage were used in the analysis and NR differences are computed from wavelength-averaged means, as well as wavelength by wavelength (spectral) means. Both methods yield virtually the same result. Figure 11b shows the overall comparison results before and after calibration, where radiometric errors have dropped to an average order of 0.8% relative to the NM over all NR levels after calibration. For bright radiances >5 W cm^{-3} sr^{-1}, the mean difference of NR is ~0.5%, remaining within the operational radiance calibration requirement of <2%. For radiances <3 W cm^{-3} sr^{-1}, the difference becomes slightly greater than 1% and tend to occur at high solar zenith angles, as might be expected from stray light contamination of the NM radiances (Chen and Jaross, 2014).

6. Summary and Conclusions

OMPS NP spectrometer on-orbit spectral performance has been well calibrated accordingly with the sensor in-flight spectral characterization. A routine bi-weekly spectral calibration now has been implemented via NP solar observation to correct spectral drifts and minimize the observed spectral uncertainty. As a result, significant improvement has been made to optimize NP spectral performance. The solar spectra uncertainty is calibrated to less than 1.8% by removal of three error sources: wavelength shifts, solar activity, and the working diffuser degradation. Validation of the radiometric accuracy of NR in the most sensitive spectral region where it has a large error has demonstrated compliance with the sensor performance requirement of 2% uncertainty. Lessons learned from the NP spectral calibration apply to the NP successors and present reasonable and feasible opportunities for improving the NP data products for the next four series JPSS satellites in the near future.

References

Chen, G., & Jaross, G. (2014). SNPP OMPS nadir instruments stray light corrections. In *STAR JPSS Annual Science Team Meeting*. Retrieved from http://www.star.nesdis.noaa.gov/star/documents/meetings/2014JPSSAnnual/dayTwo/04_Session4c_Chen_Stray_Light_Correction.pdf

Dittman, M. G., Ramberg, E., Chrisp, M., Rodriguez, J. V., Sparks, A. L., Zaun, N. H., … Wasinger, D. (2002). Nadir ultraviolet imaging spectrometer for the NPOESS Ozone Mapping and Profiler Suite (OMPS). In *Proceedings Volume 4814: Earth Observing Systems VII Earth Observing System*. https://doi.org/10.1117/12.453748

Heath, D. F., & Schlesinger, B. M. (1986). The Mg 280-nm doublet as a monitor of changes in solar ultraviolet irradiance. *Journal of Geophysical Research*, 91(D8), 8672–8682. https://doi.org/10.1029/JD091iD08p08672

Jaross, G., Cebula, R., DeLand, M., McPeters, R., Hilsenrath, E., & Krueger, A. (1998). Backscatter ultraviolet instrument solar diffuser degradation. *Proceedings of SPIE*, 3427, 432–444.

NOAA/STAR, OMPS NADIR profile algorithm theoretical basis document (2014). Retrieved from https://www.star.nesdis.noaa.gov/jpss/documents/ATBD/D0001-M01-S01-005_JPSS_ATBD_OMPS-NP-Ozone_A.pdf

Pan, C., & Flynn, L. (2015). Solar observation of Ozone Mapping and Profiler Suite nadir system during the first 3 years of on-orbit operation. *Journal of Applied Remote Sensing*, 9(1). https://doi.org/10.1117/1.JRS.9.094095

Pan, C., Flynn, L., Buss, R., Wu, X., Yu, W., & Grotenhuis, M. (2014). Performance monitoring of the S-NPP ozone mapping and profiler suite's sensor data records. *IEEE J-STARS*, 7(5), 1763–1770. https://doi.org/10.1109/JSTARS.2014.2319738

Pan, C., Flynn, L., Wu, X., & Buss, R. (2014). Suomi National Polar-orbiting Partnership Ozone Mapping Profiler Suite Nadir instruments in-flight performance. *Journal of Applied Remote Sensing*, 8(1), 30. https://doi.org/10.1117/1.JRS.8.083499

Pan, C., Kowalewski, M., Buss, R., Flynn, L., Wu, X., Capani, M., & Weng, F. (2013). Performance and calibration of the nadir Suomi-NPP Ozone Mapping Profiler Suite from early-orbit images. *IEEE IEEE J-STARS*, 6(3), 1539–1551. https://doi.org/10.1109/JSTARS.2013.2259144

Pan, C., Weng, F., Beck, T., Flynn, L., & Ding, S. (2017). Recent improvements to Suomi NPP Ozone Mapper Profiler Suite nadir mapper sensor data records. *IEEE Transactions on Geoscience and Remote Sensing*, 99, 1–7. https://doi.org/10.1109/TGRS.2017.2714103

Pan, C., Wu, X., & Flynn, L. (2013). S-NPP Ozone Mapper Profiler Suite nadir sensor performance. Retrieved from https://www.star.nesdis.noaa.gov/jpss/documents/AMM_All/OMPS_SDR/Validated/20131219-Review/Pan_OMPS_Perf.pdf

Rodriguez, J. V., Seftor, C. J., Wellemeyer, C. G., & Chance, K. (2003). An overview of the nadir sensor and algorithms for the NPOESS Ozone Mapping and Profiler Suite (OMPS), Proc. SPIE 4891. *Optical Remote Sensing of the Atmosphere and Clouds III*, 65. https://doi.org/10.1117/12.467525

Snow, M., Weber, M., Machol, J., Viereck, R., & Richard, E. (2014). Comparison of Magnesium II core-to-wing ratio observations during solar minimum 23/24. *Journal of Space Weather and Space Climate*, 4(A04). https://doi.org/10.1051/swsc/2014001

Woods, T. N., Prinz, D. K., Rottman, G. J., London, J., Crane, P. C., Cebula, R. P., … Reiser, P. A. (1996). Validation of the UARS solar ultraviolet irradiances: Comparison with the ATLAS 1 and 2 measurements. *Journal of Geophysical Research*, 101(D6), 9541–9569. https://doi.org/10.1029/96JD00225